

NUMERICAL SIMULATIONS OF A SELF-GRAVITATING, ISOTHERMAL,
PLANAR ATMOSPHERE

ELIAS RUBIN

A JUNIOR PAPER
PRESENTED TO THE FACULTY
OF PRINCETON UNIVERSITY
IN CANDIDACY FOR THE DEGREE
OF BACHELOR OF THE ARTS

RECOMMENDED FOR ACCEPTANCE
BY THE DEPARTMENT OF
ASTROPHYSICAL SCIENCES

ADVISERS: EVE OSTRIKER & AARON SKINNER

JANUARY 5, 2016

I hereby declare that I am the sole author of this thesis.

I authorize Princeton University to lend this thesis to other institutions or individuals for the purpose of scholarly research.

Elias Rubin

I further authorize Princeton University to reproduce this thesis by photocopying or by other means, in total or in part, at the request of other institutions or individuals for the purpose of scholarly research.

Elias Rubin

ABSTRACT

We describe the results from a set of numerical simulations of a self-gravitating, isothermal, planar atmosphere. We evolve the equations of radiation hydrodynamics (RHD) using the *Hyperion* code. Our simulations are parametrized by the opacity of the gas κ , the surface density of the atmosphere Σ , and the fraction of total mass fixed at the midplane ϵ_* . We explore a range of values for κ , which is the most important parameter in determining the dynamics of the cloud. We observe two solution regimes in the limits of $\kappa < 17$, where the radiation is not sufficiently powerful to drive significant mass outflows in the gas, and $\kappa > 20$, where almost all of the gas is rapidly ejected from the simulation domain. Although we have difficulty sampling this intermediate regime due to an unphysical decoupling of the gas from the fixed mass in for $17 < \kappa < 20$, we posit that opacities in that intermediate range may correspond to significant turbulence which may drive limited outflows. Future work on this problem must investigate this intermediate regime to asses the viability of reprocessed radiation as a candidate for driving significant outflows in giant molecular clouds.

1. Introduction

Giant molecular clouds (GMCs) are prolific star forming regions. However, the overall rates of star formation in GMCs are small. The star formation efficiency in a typical GMC is about 1%. The dynamics of these regions are complex, and cannot effectively be evaluated analytically, so it is necessary to perform numerical simulations to gain insight into their solutions. There has also been discussion (see, e.g., Davis et al. 2014), of the effectiveness of varying numerical methods for modeling these regions, comparing

the effectiveness of flux-limited diffusion (FLD) and variable Eddington tensor (VET) methods. In this paper, we conduct idealized, two-dimensional, numerical simulations of an isothermal, self-gravitating, full-planar atmosphere to model the dynamics of gas near the disk of a cloud, using the *Athena* code of Skinner & Ostriker (2013) and employing the M_1 closure. We examine the effects of varying the opacity κ and the fraction of mass fixed to the planar source ϵ_* .

The plan of this paper is as follows. In Section 2, we offer a brief overview of the theoretical and observational background behind this paper, and examine recent work on the effects of reprocessed radiation on giant molecular cloud (GMC) dynamics. In section 3, we discuss our numerical methods. In section 4, we explain what differentiates our model from previous work as well as our choice of parameters. In section 5, we look at the outcomes of our numerical simulations and discuss their meaning. Finally, in section 6, we summarize and discuss the paper.

2. Literature

Recent research has shown promising results for explaining the low star formation efficiency in molecular clouds. In this section we examine evidence for our explanation of choice – reprocessed radiation feedback as the driver of turbulent outflows from GMCs – and review previous simulations of similar problems to ours. We also sketch a brief overview of the general theory background and observational evidence which informs our research.

2.1. Star Forming Regions and Star Formation

Star formation occurs in regions of interstellar space when gas clouds collapse. Kippenhahn et al. (2012) offers a succinct summary of our modern idea of star formation –

that turbulent shocks and flows in the clouds of molecular gas which are most associated with star formation (Krumholz 2014; Leroy et al. 2008) cause fragmentation and clumping into smaller, gravitationally unstable structures, which then collapse into stars. Molecular gas clouds, also known as H₂ regions, tend to be located more towards the center of galaxies and typically have surface densities Σ such that $\Sigma > 10 M_{\odot} \text{ pc}^{-2}$. Figure 1 shows a mapping of molecular gas and star formation suggesting that most star formation occurs in molecular clouds. The time scale of star formation is characterized by a depletion time (Krumholz 2014), $t_{\text{dep}} \equiv M_{\text{Gas}}/M_*$, which, for molecular clouds with $\Sigma > 10 M_{\odot} \text{ pc}^{-2}$, tends to be on the order of ~ 1 Gyr. This depletion time can be compared to the dynamical time of the gas cloud, the most natural choice of which is the free-fall time, which for a spherical cloud is

$$t_{\text{ff}} = \sqrt{\frac{3\pi}{32G\rho}} \quad (1)$$

which, depending on the densities, tends to range from $\sim 1 - 10$ Myr (Krumholz 2014). Most gas clouds fall close to the line $t_{\text{ff}}/t_{\text{dep}} \equiv \epsilon_{\text{ff}} \approx 0.01$, that is, the depletion time is about 100 times longer than the dynamical time of the cloud (Krumholz 2014). This fraction tells us that star formation is globally inefficient in clouds. If it were not, we would expect $\epsilon_{\text{ff}} \approx 1$, that is all of the gas in the cloud would form stars in one free-fall time. The overall star formation efficiency factor now is $\approx 1\%$ (although there is evidence that suggests it was greater in the early universe) (see Mac Low & Klessen 2004, and references therein).

The natural question to ask is what limits the efficiency in local clouds. The internal support predominantly seems to come from turbulence (Mac Low & Klessen 2004) which simultaneously causes overdense areas which collapse into stars and disperses other regions which prevents star formation. The cause of this turbulence remains an open question. Krumholz (2014) argues that supernova feedback is unlikely to sufficiently limit the star

formation rate especially in smaller clouds where supernovae occur relatively infrequently, nor early in the life of the cloud when no supernovae have yet occurred.

2.2. Reprocessed Radiation as Primary Feedback Mechanism

Radiation pressure from stars on dust grains is a promising driving mechanism for turbulence, but there is still an open discussion as to the ability of radiation pressure to significantly disrupt star formation in GMCs or to drive outflows on galactic scales. Krumholz & Thompson (2012) (hereafter KT12) suggest that the momentum exchange rate of radiation pressure is not sufficient to drive the levels of turbulence which are observed in mature clusters. However, other authors suggest that reprocessed radiation may be able to drive substantial turbulence and mass outflow (Davis et al. 2014; Skinner & Ostriker 2015; Rosdahl et al. 2015), at least for some regions of the parameter space, especially when the optical depth is large. Skinner & Ostriker (2015) demonstrate that radiation feedback can significantly inhibit star formation for $\kappa = 20 - 40 \text{ cm}^2 \text{ g}^{-1}$, but such high opacities are likely not typical. Davis et al. (2014) run half-plane numerical simulations without self-gravity which show some outflow, but suggest that outflow and regions of increased turbulent velocity are more plausible in a model with self-gravity. Davis et al. (2014) also posit that even in a cloud with a lower overall optical depth, turbulence in regions of the gas with a high optical depth may be sufficient to drive the overall evolution of the system.

2.3. Krumholz and Thompson - FLD Simulation

The model of KT12, which we follow with a few important variations, is an idealized half-plane solution for a radiating disk. They use the ORION radiation hydrodynamics (RHD) code which is in most respects similar to the *Hyperion* solver of Skinner & Ostriker (2013).

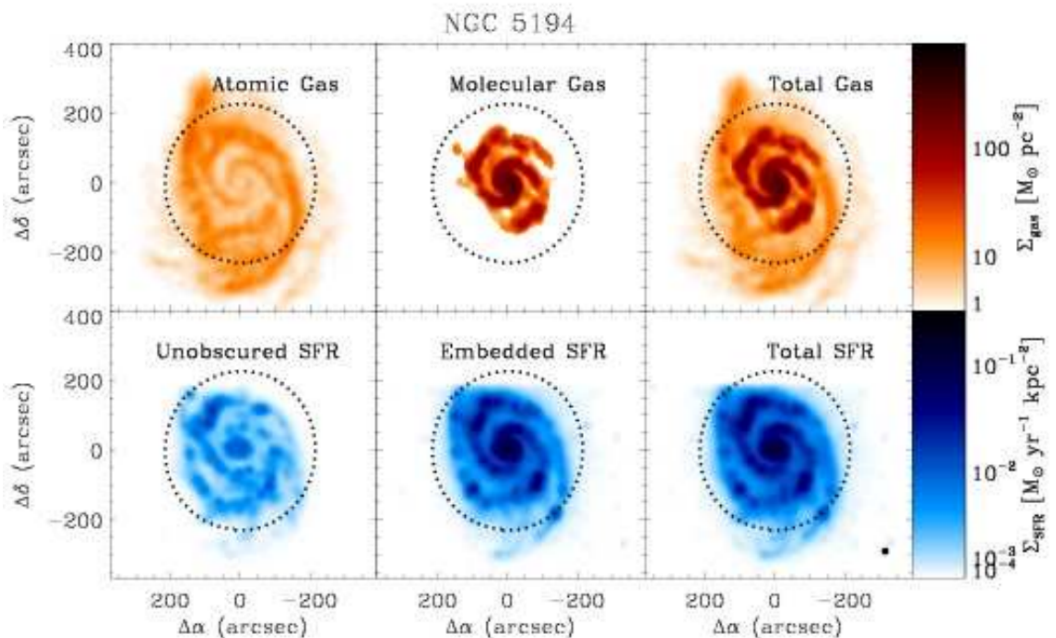


Fig. 1.— This figure, reproduced from Leroy et al. (2008), shows observational data from the galaxy NGC 5194. The atomic gas distribution in the upper left panel is traced via the 21 cm hydrogen spin-flip transition line and the molecular gas distribution in the upper middle panel is traced via the CO $J = 1 \rightarrow 0$ rotational transition line. The upper right panel is a superposition of the two. The unobscured star formation rate (SFR) in the lower left panel comes from direct ultraviolet observations and the embedded SFR is inferred by observation of the 24 micron infrared emission line, corresponding to the reemission of ultraviolet light reprocessed by dust. We can see that the embedded SFR is greater by 1-2 orders of magnitude and corresponds with the locations of increased H₂ densities.

KT12 implement a constant gravitational force per unit mass, $-g\hat{z}$, and a constant radiation flux, $F = F_0\hat{z}$, imposed on the boundary at $z = 0$. They also implement a temperature-dependent opacity function, so the opacity is not constant throughout the simulation, with reflecting boundary conditions for the gas at the mid-plane, outflow boundary conditions for both the gas and radiation at the upper- z boundary, and periodic boundary conditions in the horizontal direction.

The other important difference between the model of KT12 and others is their use of the FLD method. This method leads to a strong flux-density anti-correlation, as shown in Figure 2, which manifests because the FLD scheme relates the radiation flux \mathbf{F} to the gradient of the radiation energy density E_r as

$$\mathbf{F} = -\frac{c\lambda}{\kappa\rho}\nabla E_r, \quad (2)$$

where κ is the opacity, ρ is the gas density, and λ is the flux-limiter, the details of which are given in KT12. The results of Davis et al. (2014) go on to show that this anti-correlation stems from the tendency for radiation in the FLD method to “leak” through low-density channels, and is not reproduced to nearly the same extent with their more accurate VET method.

2.4. Davis et. al - VET Simulation

The VET method used by Davis et al. (2014) offers significantly higher fidelity to the geometry of the underlying radiation field compared to FLD, but at a higher computational cost. There is not any way to increase the accuracy of FLD outside the optically thick limit. Davis et al. (2014) aim first to reproduce the FLD results of KT12 and then compare them to a reproduction of the same model using the VET integration scheme. Davis et al. (2014) show that the two models yield similar results in the stable parameter regime when f_{Edd} is

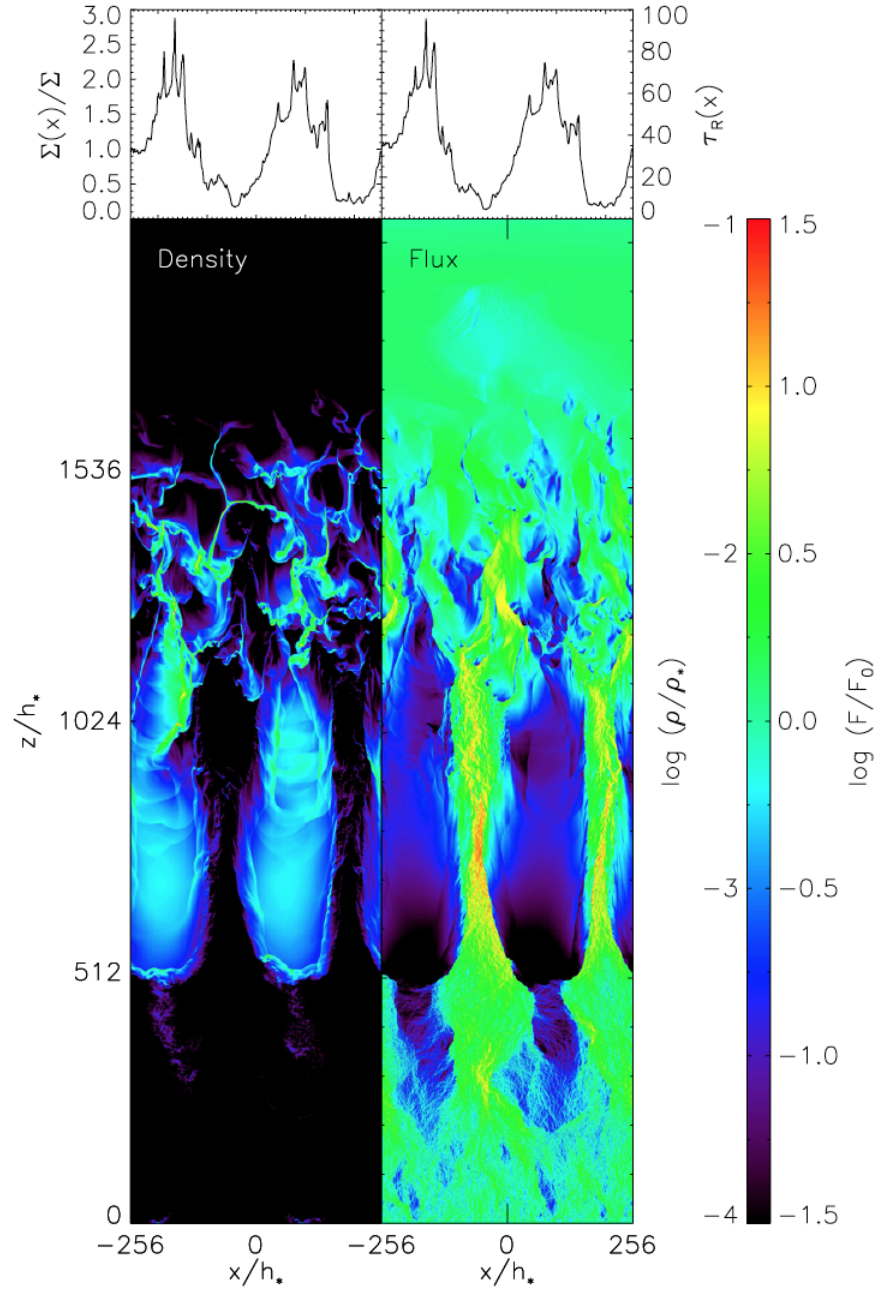


Fig. 2.— This figure, reproduced from Krumholz & Thompson (2012), shows the anti-correlation between the gas density and radiation flux in their FLD-based simulations. The radiation tends to go into the low-density channels, escaping out of the top of the simulation and reducing the radiation force on the gas.

small, but that in the unstable regime where f_{Edd} is larger but still less than 1, the average radiation force is significantly higher because it is not artificially constrained. This results in a reduced anti-correlation between gas and radiation, as shown in Figure 3, resulting in stronger turbulence.

2.5. Skinner and Ostriker - M_1 Simulation

Rather than continuing to reproduce the planar structure of KT12, Skinner & Ostriker (2015) consider three-dimensional clouds with embedded radiating star particles. They use a two-moment method and employ the M_1 closure, which does not offer the same degree of angular resolution as the VET method, but is significantly faster and less expensive. These clouds model embedded super star clusters in GMCs, which are massive enough to fully sample the initial mass function (IMF). The model employs self-gravity and luminous star particles which can accrete mass in order to represent star formation. The simulations show the opacity κ is the most important parameter for determining the evolution of the cluster. An opacity $\kappa > 15$ is sufficient to drive significant outflows, but beneath that level there is little driving from radiation. Skinner & Ostriker (2015) show a lesser dependence on the surface density Σ , with lower Σ leading to somewhat reduced star formation efficiencies due to a shallower potential well. They also stress the need to check the M_1 method against other methods, such as VET and Monte Carlo.

All of this past work suggests that we ought to expect κ to be a key parameter in controlling the dynamics of our simulations. We should expect the use of the M_1 closure to bring some more accuracy as compared to FLD, but we are also not replicating the experiment of KT12 exactly. The specifics of our model are described more fully in Section 4.

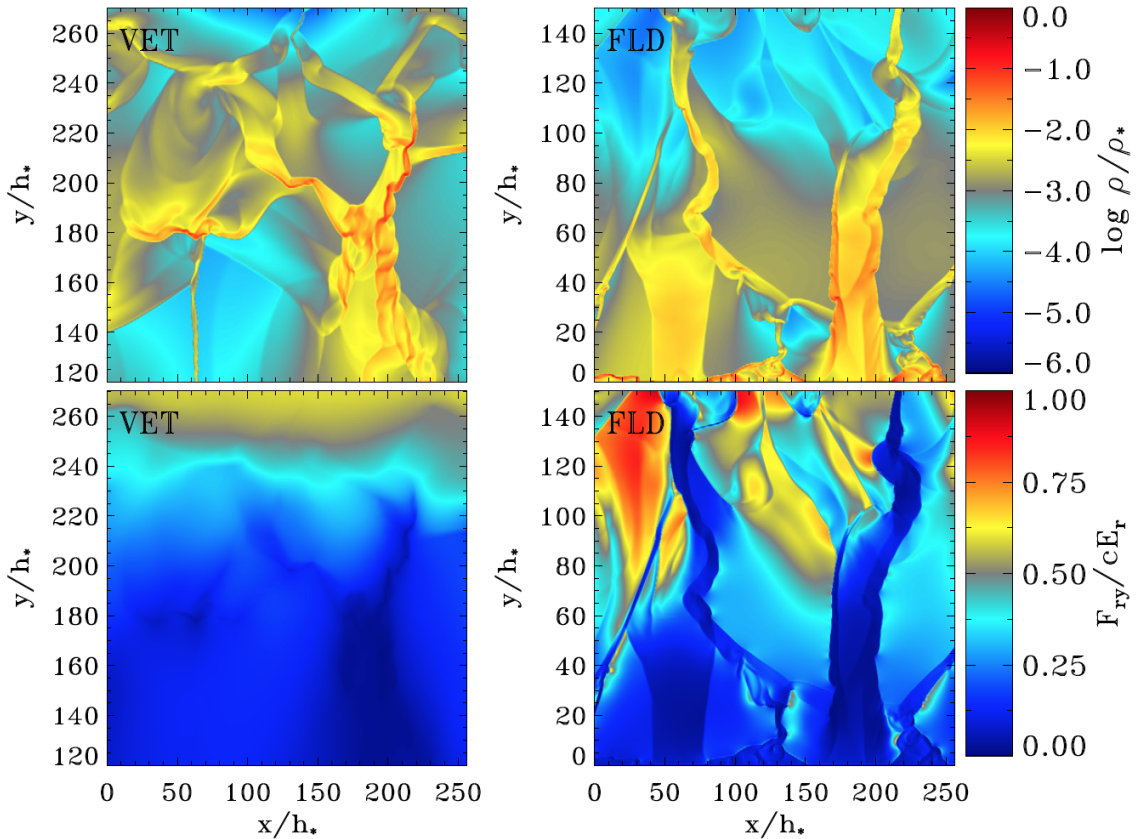


Fig. 3.— This figure, reproduced from Davis et al. (2014), compares the flux-density anti-correlation between their VET and FLD simulations for the same run. The top row of figures is the gas density in each simulation and the bottom row is the ratio of vertical radiation flux to radiation energy density. The pronounced channel structure in the FLD run is still present in the VET run, but the radiation is not so strictly limited to the channels, leading to a weaker anti-correlation.

3. Methods

Our numerical experiments are implemented using the *Hyperion* code, (Skinner & Ostriker 2013), an extension of the *Athena* code of Gardiner & Stone (2008). *Hyperion* is a grid-based RHD code which uses both implicit and explicit finite volume methods to solve the RHD equations. *Hyperion* also employs the M_1 closure relation (Levermore 1984) which closes the moment hierarchy after the second-order moment. We make a number of approximations in the name of computational efficiency and feasibility. Many of these approximations are explored more fully in Skinner & Ostriker (2013), but we will address them here nonetheless.

3.1. The M_1 Closure Relation

We employ the M_1 closure, which was originally proposed by Levermore (1984). The M_1 closure exactly describes the limits of optically thin, streaming radiation and optically thick, diffusing radiation, but is also effective in intermediate regimes. The M_1 closure provides a significant increase in physical fidelity over the commonly used FLD approximation. FLD approximations tend to become unphysical where shadowing occurs, as the radiative flux follows the local gradient of the energy density. In our simulations we expect to see shadowing because turbulence leads to clumpy structures in the gas. Thus, FLD methods would actually cause the radiation to go almost exactly where it should not. VET methods have also been employed to solve RHD problems (see, e.g., Davis et al. 2014). Although accurate, these methods are very computationally expensive, and are not particularly suited for exploring a large parameter space. Although the M_1 relation is itself more computationally expensive than FLD, we believe it is worth the cost, because without it, the results would fairly uninformative.

3.2. Reduced Speed of Light Approximation

The diffusion of radiation typically occurs on a significantly shorter timescale than the movement of the gas. However, to preserve the dynamics of the system, we simply require that \hat{c} , the radiation propagation speed $\hat{c} \gg v_{\max}$, where v_{\max} is the maximum hydrodynamic signal speed, i.e., $\max\{|\mathbf{v}| + c_s\}$. As originally proposed by Gnedin & Abel (2001), we adopt the reduced speed of light approximation (RSLA), where \hat{c} is the reduced speed of light. In the non-relativistic regime, this can be achieved with $\hat{c} \ll c$. The computational cost savings of this approximation are enormous. It allows us to compute far fewer explicit radiation cycles per gas cycle while maintaining the physical fidelity of the dynamics. Using the RSLA, the ratio of radiation integration steps to gas integration steps is given by the optical depth $\tau_{\max} = \hat{c}/v_{\max}$, which for our simulations is on the order of about 20. The fiducial value of τ is given by

$$\tau \approx \frac{1}{2} \left(10^3 \frac{M_\odot}{\text{pc}^3} \right) \left(10 \text{ cm}^2 \text{ g}^{-1} \right) \left(\frac{\Sigma}{100 M_\odot \text{ pc}^{-2}} \right) \left(\frac{\kappa}{10 \text{ cm}^2 \text{ g}^{-1}} \right) \quad (3)$$

This also means that we don't have to compute the evolution of the gas equation on the radiation timescale, where it essentially doesn't do anything.

3.3. Integrators

The system of equations to be solved for the gas and radiation is given by

$$\partial_t \rho + \nabla \cdot (\rho v) = 0, \quad (4a)$$

$$\partial_t \rho v + \nabla \cdot (\rho v v + P \mathbb{I}) = -\rho \nabla (\Phi_* + \Phi_{\text{gas}}) + \rho \kappa \frac{\mathbf{F}}{c}, \quad (4b)$$

$$\frac{1}{\hat{c}} \partial_t \mathcal{E} + \nabla \cdot \left(\frac{\mathbf{F}}{c} \right) = \frac{j_*}{c}, \quad (4c)$$

$$\frac{1}{\hat{c}} \partial_t \left(\frac{\mathbf{F}}{c} \right) + \nabla \cdot \mathbb{P} = -\rho \kappa \frac{\mathbf{F}}{c}, \quad (4d)$$

where ρ , v , and P are the gas density, velocity, and pressure, respectively, and Φ_{gas} and Φ_* are the gravitational potential of the gas and static source term. \mathcal{E} , \mathbf{F} , and \mathbb{P} are the frequency-integrated radiation energy density, flux vector, and pressure tensor, respectively (Skinner & Ostriker 2015). \hat{c} is the reduced speed of light, κ is the absorption opacity of the gas, and j_* is the radiation source term.

Because the integration of the gas equation is decoupled from that of the radiation equation, we are able to operator split the integrators for gas and radiation. To evolve the gas equations we use the van Leer (VL) integrator of *Athena* (Stone & Gardiner 2009) which is a high-order Godunov method. For hydrodynamics, we use the minimally-diffusive HLLC Riemann solver, (Batten et al. 1997; Toro 1997). The VL integrator and HLLC solver provide second-order accuracy at a relatively low computational cost, which makes them an effective choice for our problem. The radiation equations are also evolved with an HLL-type integrator, the details of which are described in Skinner & Ostriker (2013). This Riemann solver provides the advantage of being unconditionally stable. In the integrator we also impose the condition of radiative equilibrium, which states that any radiation which is emitted by gas is immediately locally reabsorbed.

3.4. Self-Gravity

Our model is differentiated from experiments such as those in Krumholz & Thompson (2012) by the use of self-gravity. We employ disk gravity (Gong & Ostriker 2013), which acts along the z -axis, as well as a static potential from the mass of the source at the midplane. There is not an analytic solution for the initial density distribution when considering both the self-gravitational potential and the static potential from the source. We instead numerically compute a one-dimensional, relaxed solution of the gas density in the absence of radiation and use this as the initial condition for the density distribution. The disk gravitational potential is given by

$$\nabla^2 \Phi_{\text{gas}} = 4\pi G \rho(z), \quad (5)$$

and implemented with FFTs, with vacuum boundary conditions in the vertical direction and periodic boundary conditions in the horizontal direction.

3.5. Radiation Source Profile

Our radiation source is positioned at the midplane and extends in both the positive and negative z -directions. We extend the radiation source over the grid as a Gaussian with a half width of four grid zones, so it can form a self-consistent radiation flux. This Gaussian is then copied along the x -axis, so the source is uniform along the plane. In our high-resolution simulations, this is essentially a δ -function, extended over the transverse direction. Radiation energy is injected onto the grid at each time step from this source term. In our model the luminosity of the source is constant with time as described in Section 4, but it would be relatively simple to implement a time-dependent source term.

3.6. Density Floor and Cleanup

Because the integrator chooses its timestep based on the maximum velocity of the gas, low-density gas with high momentum can cause the time step to plummet, effectively halting the integrator. When this occurs in some zone, we apply a density floor and reset the momenta there to zero. Our choice for the density floor is $\rho_{\min} = 10^{-5}\rho_0$, where ρ_0 describes the midplane density. This density floor keeps the timestep in a reasonable range without significantly affecting the total mass or momentum. The density floor is applied after each gas cycle.

3.7. Parallelization Support and Scaling

The *Athena* code is parallelized via MPI (Stone et al. 2008). *Athena* uses standard domain decomposition to split the domain into independent MPI grids. Ghost zones are used at the boundary of each MPI grid to reconstruct the variables at each full timestep. MPI allows scaling to arbitrarily high resolutions, although the number of processors required to perform simulations in reasonable amounts of time can quickly become large. Doubling the zones in either the x or z direction halves the simulation timestep, so doubling both the number of zones in the x and z directions causes approximately an 8-fold increase in computation time for the same physical time.

4. Model

In this section we describe our model and parameters. We explore our choice of parameters, the relationships between them, and the physical ranges of these parameters. We also describe the specifics of our model and how it differs from previous work. Finally, we enumerate the parameters we use for our experiments.

4.1. Physical Parameters

Our model is described by five physical parameters: the isothermal sound speed, c_s ; the total surface density, Σ ; the fraction of mass fixed to the planar source, ϵ_* ; the specific luminosity of the source, Ψ and the opacity of the gas, κ . Although we are free to change all of these parameters, we adopt characteristic values for some so as to narrow the parameter space. We set $c_s = 1000 \text{ km s}^{-1}$ and $\Psi = 2000 \text{ erg s}^{-1} \text{ g}^{-1}$, which are, respectively, typical values of the sound speed in GMCs and of the specific luminosity of hot, young, massive clusters. We also note that Ψ and κ only appear as a product in f_{Edd} , so varying κ is sufficient to sample both.

4.2. Full-Plane Solution

Our model is a two-dimensional planar, atmosphere, centered at the midplane. We adopt the convention that z is the vertical direction and x is the transverse direction. During the initialization process, we compute $H_\infty \equiv c_s^2/g_\infty$, the atmospheric scale height as $z \rightarrow \infty$, where g_∞ is the total gravitational acceleration as $z \rightarrow \infty$. In all of our simulations, the simulation box typically extends at least 10 effective scale heights in the positive and negative z direction, and 2.5 scale heights in the positive and negative x direction, where the effective scale height is $H_{\text{Eff},\infty} \equiv H_\infty/(1 - f_{\text{Edd},\infty})$. The extent in the x -direction is significantly less than the Jeans length, and so we are not subject to gravitational fragmentation. Our simulation time is parametrized by the crossing time for one scale height, $t_{\text{cross}} = H_\infty/c_s$, and simulations are typically evolved to 250 t_{cross} . The full-plane solution provides a significant advantage over the previously used half-plane solution outlined in KT12, because we are able to use the same boundary conditions for both the upper and lower z -boundaries. In contrast, the half-plane solution imposes an unphysical reflection boundary condition on the gas and radiation at the source.

4.3. Boundary Conditions

We enroll outflow boundary conditions for both the radiation flux and gas in the z -direction, and periodic boundary conditions for all variables in the x -direction. We also enroll a gradient boundary condition on the radiation energy density in the z -direction. The periodic boundary conditions thus model a plane which is infinitely extended in the x -direction. The outflow boundary conditions mean that as gas and radiation reach the upper and lower boundaries of the grid they are ejected and are unable to return. Most of the ejected gas is moving at well over the escape velocity, so we do not expect there to be significant losses of unbound gas that would otherwise fall back.

4.4. Isothermal Equation of State

We employ an isothermal equation of state (EOS). This EOS is a simplification, but a reasonable one, because the sound speed is small in comparison to the expected turbulent velocities. If the sound speed in the gas were sufficiently high, it would be necessary to use an adiabatic equation of state, which would involve implementing a temperature-dependent opacity function.

4.5. Stationary source

Our radiation source is centered at the midplane. We model the source as a Gaussian with a half-width at half-maximum (HWHM) of four grid zones. When the resolution is sufficiently high, the width of the source is narrow compared to the width of the gas distribution and so it behaves as a δ -function. The radiation flux from the source is given

by

$$j_* = \frac{\epsilon_* \Sigma \Psi}{\sqrt{2\pi\sigma^2}} \exp \frac{z^2}{2\sigma^2}, \quad (6)$$

where $\sigma = 4\Delta z / 2 \ln 2$. There is no time dependence of the source term, but the energy density of radiation steadily increases, as not all of the radiation can leave the simulation box in a given hydrodynamical timestep. We also assume our model occurs in the limit of radiative equilibrium, where radiation emitted by gas is immediately reabsorbed locally. This means that the only radiation source is from our planar source term, rather than from numerous source particles that can move throughout the gas, which simplifies the computation. We model only the infrared (IR) radiation reprocessed by dust in the atmosphere in the disk.

4.6. Bound Mass at the Midplane

Because the radiation source term is fixed to the midplane and not to the center of mass of the gas, we require some amount of mass be bound to the midplane. Without doing so, for strong radiation fields, the center of mass of the gaseous system would be decoupled from the radiation source and begin to move along the z -axis. We introduce the parameter ϵ_* , which allows us to decide how much mass to bind to the midplane. The bound mass is essentially equivalent to a uniform distribution of stars positioned at the midplane. We introduce a static potential from the bound mass, which adds to the self-gravitational potential of the gas in order to form the full potential. The static potential is given as a function of z by

$$\Phi_*(z) = 2\pi G \epsilon_* \Sigma |z| \quad (7)$$

Our tests have shown that this static potential is sufficient to keep the bulk of the gas appropriately centered around the source.

4.7. Initialization

Because there is not an analytic form for the equilibrium gas density profile corresponding to the combined static and self-gravitational potentials, we instead relax from an approximate solution. In the absence of the static potential, i.e., for $\epsilon_* = 0$, the self gravitating gas should go as

$$\rho(z) = \rho_0 \operatorname{sech}^2(\alpha z), \quad (8)$$

where

$$\rho_0 = \frac{\pi G(1 - \epsilon_*)^2 \Sigma^2}{2c_s^2} \quad (9)$$

and

$$\alpha = \frac{\sqrt{2\pi G\rho_0}}{c_s}. \quad (10)$$

For the case $\epsilon_* \neq 0$, this solution is allowed to relax in one dimension in the absence of radiation. The one-dimensional, relaxed density is then used as the initial vertical density profile in the two-dimensional simulation by replicating the one-dimensional profile in the transverse direction. We also introduce velocity perturbations into the gas. We use a perturbation strength of $\epsilon_{\text{turb}} = 0.2$ across all simulations, which corresponds to a moderate but not at all unusual velocity distribution. We can randomize these perturbations across trials but generally used a fixed random seed. The perturbations are distinct across different MPI grids - we do not copy the same perturbations across.

We follow Skinner & Ostriker (2015) in our use of Gaussian random perturbations with power spectrum $|\delta\mathbf{v}| \propto k^{-4}$, for $k/dk \in [2, 64]$, where $dk = 2\pi/L_x$. The perturbations are normalized such that there is no net momentum added to the domain, and are always the same for a given random seed, regardless of the number of MPI grids.

4.8. Observables

We are most interested in learning about the mass history of our simulations. Is mass ejected from the simulation, and if so, how much? Does this occur in reasonable areas of the parameter space? For a sanity check, we can look at the dimensionless Eddington factor - the ratio of radiation force outward to gravitational force inwards a particle experiences, defined as

$$f_{\text{Edd,plane}} = \frac{\Psi\kappa}{4\pi G_C}, \quad (11\text{a})$$

$$f_{\text{Edd},\infty} = \frac{\epsilon_* \Psi\kappa}{4\pi G_C}, \quad (11\text{b})$$

where $f_{\text{Edd,plane}}$ is the Eddington factor at the midplane where $\Phi_{\text{gas}} \rightarrow 0$ as $z \rightarrow 0$, which is therefore greater than $f_{\text{Edd},\infty}$. We note that in the self-gravitating atmosphere this is not the same for all z . The gravitational acceleration falls off at the midplane, and thus, the Eddington factor will vary over the simulation space. Still, we can compute the spatial average over the problem domain and observe the time evolution of $\langle f_{\text{Edd}} \rangle$, recalling that

$$\langle \bullet \rangle = \frac{1}{L_x L_y L_z} \int_{x_{\min}}^{x_{\max}} \int_{y_{\min}}^{y_{\max}} \int_{z_{\min}}^{z_{\max}} \bullet dx dy dz, \quad (12)$$

and

$$\langle f_{\text{Edd}} \rangle = \frac{\langle F_{\text{rad},z} \rangle}{\langle F_{\text{grav},z} \rangle}. \quad (13)$$

We can also visualize the density of the gas over time and qualitatively describe what happens to it. Finally, we consider ξ_{end} , the fraction of mass remaining on the grid at the end of the simulation.

4.9. Parameter Table

Run (units)	κ	Σ (M_{\odot} pc $^{-2}$)	ϵ_*	$f_{\text{Edd},\infty}$	$f_{\text{Edd,plane}}$	L_z	ξ_{end}
							(H_{eff})
E50K05s100	5	100	0.5	0.20	0.40	20	1.0
E50K10s100	10	100	0.5	0.40	0.80	20	1.0
E50K11s100	11	100	0.5	0.44	0.88	20	1.0
E50K12s100	12	100	0.5	0.48	0.96	20	1.0
E50K16s100	16	100	0.5	0.64	1.28	20	0.978
E50K18s100	18	100	0.5	0.72	1.44	30	0.0001
E60K17s100	17	100	0.6	0.816	1.36	40	0.997
E60K18s100	18	100	0.6	0.864	1.44	40	0.0005
E70K12s100	12	100	0.7	0.672	0.96	20	0.985
E70K14s100	14	100	0.7	0.748	1.07	20	0.976
E70K15s100	15	100	0.7	0.84	1.20	20	0.989
E70K155s100	15.5	100	0.7	0.868	1.24	20	0.995
E70K16s100	16	100	0.7	0.896	1.28	20	0.0003
E70K25s100	25	100	0.7	1.4	2	20	0.0001

Simulations were also conducted with $\epsilon_* < 0.5$ but were subject to a strong gas-radiation decoupling effect where the center of mass was ejected as shown in Figure ???. Extending L_z above 20 helped in reducing the decoupling effect for $\kappa = 16$ and $\kappa = 17$ because it preserved symmetries in the density field, but even E60K18S100 which had $L_z = 40$ saw decoupling, just at a later time than E50K18S100. A visualization of this decoupling effect is available at <https://goo.gl/nugY9V>. Increasing ϵ_* also helped as increased Φ_* helped to keep the gas centered.

5. Results and Discussion

In this section we present the results from the numerical experiments described in Table 4.9. We show a variety of outcomes below and above the critical value of the opacity κ_c at which there are some outflows from the system. We hypothesize the most interesting dynamics are in the intermediate range just above the critical opacity, where there are significant outflows, but the entire gas mass is not ejected. However, this range seems to be narrow in κ , and is therefore difficult to sample from, especially when confounded by the decoupling effect mentioned above. None of our runs seemed to sample this regime. Another caveat is that simulations were extended for $t_{\max} = 250t_{ff}$, so any gas which may have become unbound later than t_{\max} would not be counted as such.

5.1. The Steady-State Solution

When $\kappa < \kappa_c$, the radiation force is sufficient to drive oscillatory motion in the gas, but not outflows. The oscillations have a maximum amplitude of about $10 H_{\text{Eff},\infty}$ along the z direction, as shown by the fact that although there is gas close to the simulation boundary, no significant amount of mass leaves the domain. Figure 4 shows the typical behavior of one stable run. A visualization of the run E50K05S100 is available at <https://goo.gl/1P0uBc>. Figure 5 shows the group of the stable runs in the $\epsilon_* = 0.5$ series.

5.2. The Supercritical Limit

When $\kappa \gg \kappa_c$ such that $f_{\text{Edd},\infty} > 1$, the gas does not oscillate at all. The radiation force is strong enough to dramatically accelerate almost the all of the gas out of the atmosphere on a relatively short timescale, within $100t_{\text{cross}}$. In our simulations this manifests by bypassing the decoupling effect observed at intermediate values of the opacity around

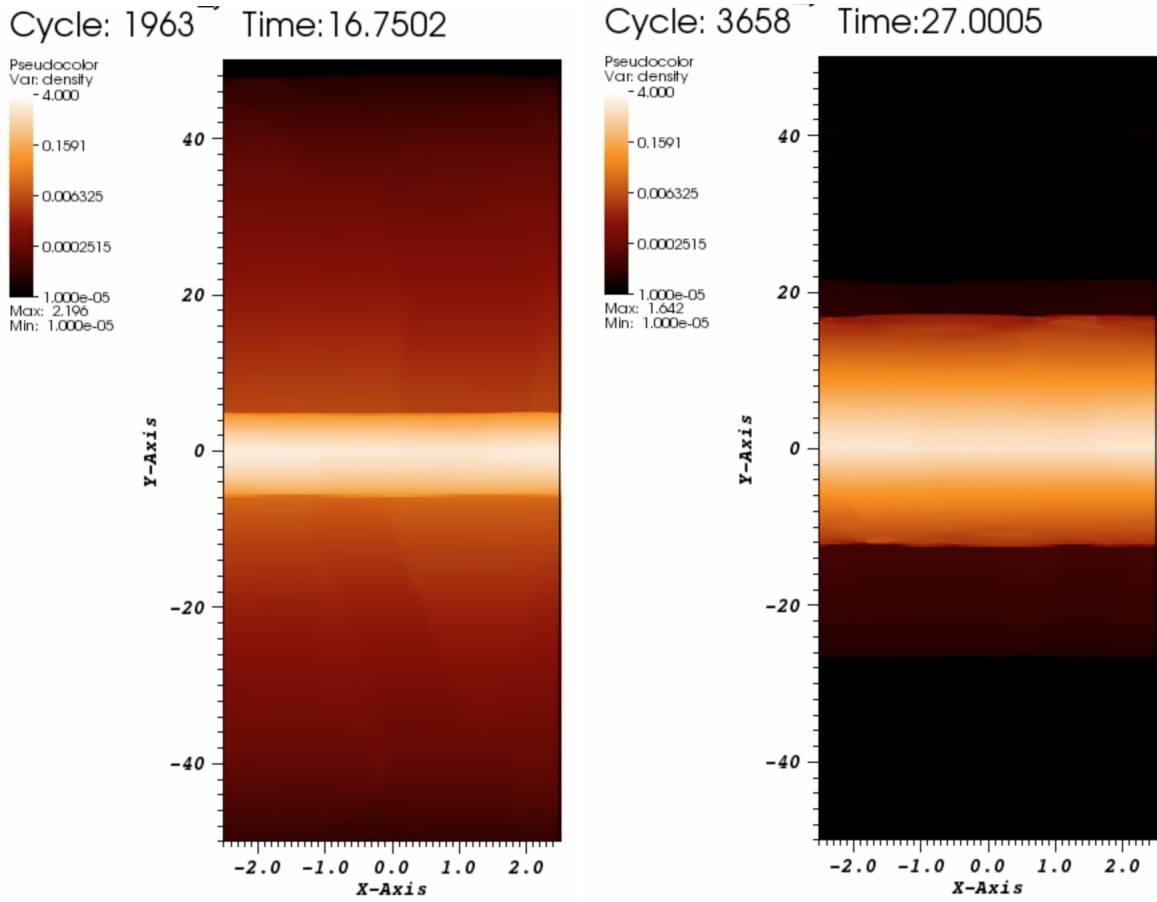
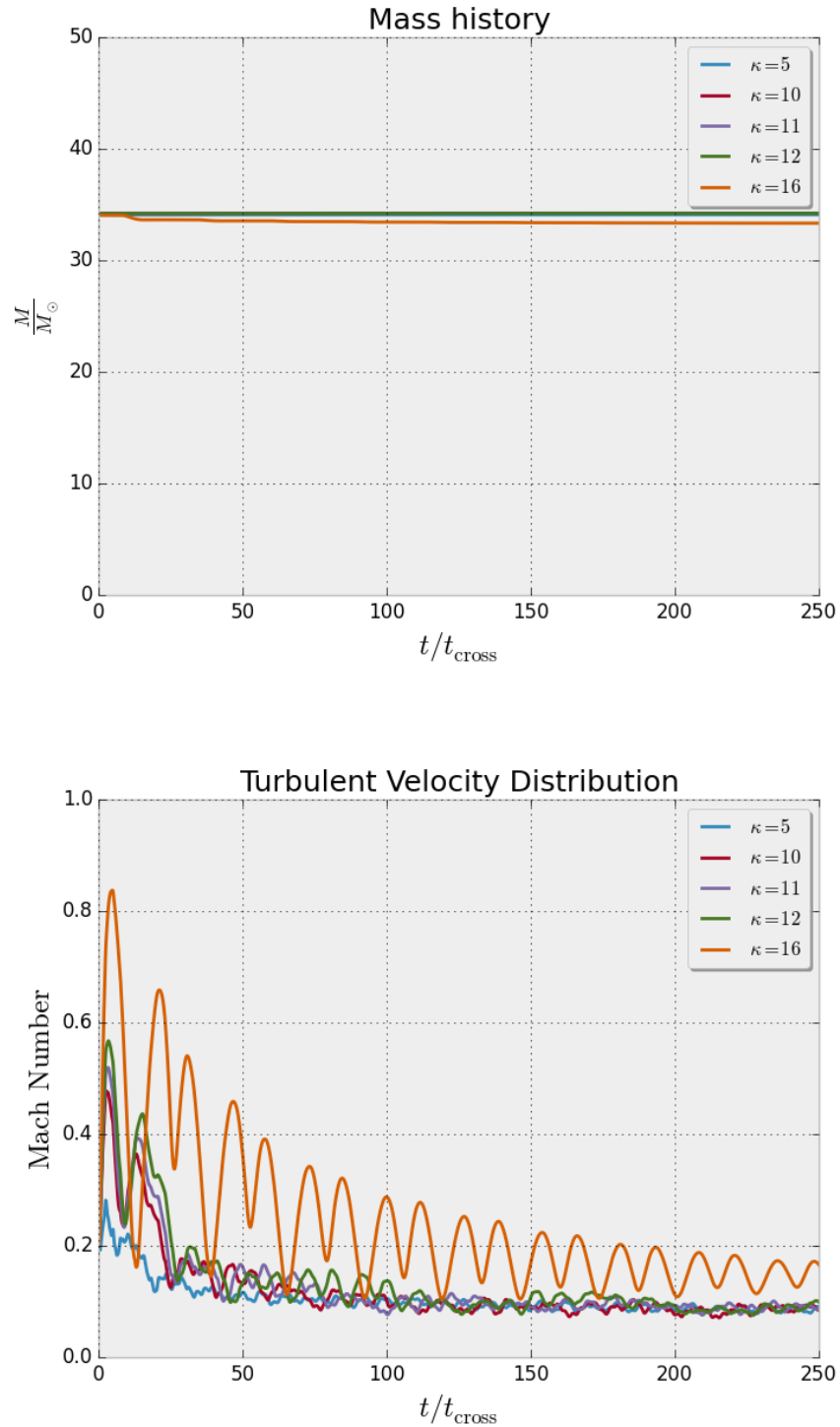


Fig. 4.— This figure, from the run E50K11S100 shows oscillatory motion in the stable case. The maximum amplitude of the oscillation is about $10H_{\text{Eff},\infty}$. The gas which reaches the boundary then falls back to the midplane, but the radiation support prevents it from becoming quite as dense as the initial condition.



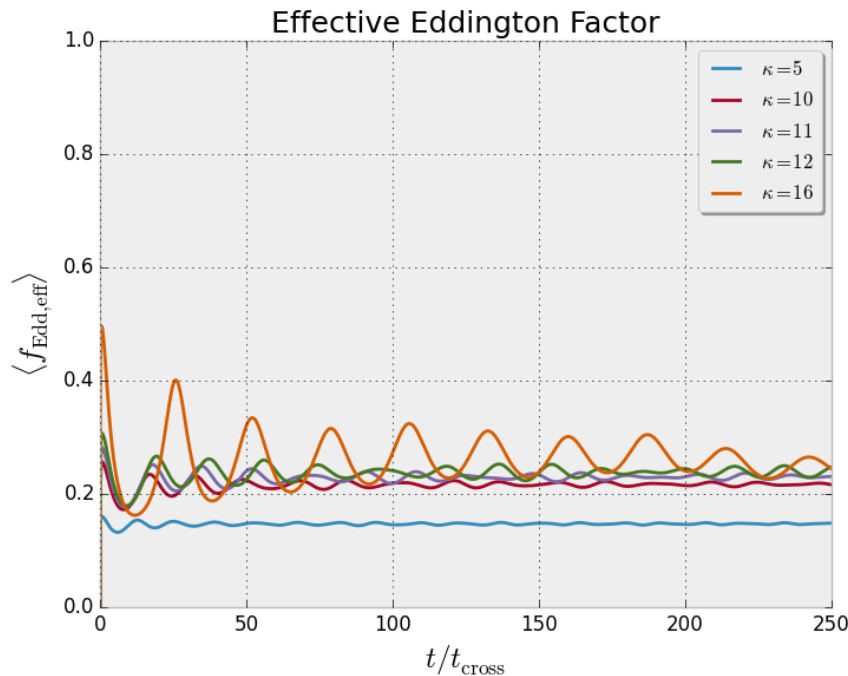


Fig. 5.— These three plots are respectively the mass history, the spatial average of the turbulent velocity, and the effective Eddington factor for the set of stable runs. The oscillatory nature of the solution is reflected in the periodic oscillations of $\langle f_{\text{Edd}} \rangle$ and the Mach number. The decaying nature of the Mach number comes from the decay of the perturbed initial condition.

$17 < \kappa < 20$. This regime where almost all of the gas is unbound is not reflected in GMCs, which, by virtue of their long lifespans, require that there remains significant amounts of gas in the cloud. Figure 6 shows a supercritical outflow when $\kappa = 25$. A visualization of that run is available at <https://goo.gl/n6h1OJ>.

5.3. The Critical Neighborhood

Although we were not able to explicitly demonstrate the existence or properties of a critical neighborhood with special behaviors, there are some results that hint at its existence. Namely, the non-oscillatory supercritical behavior in the high- κ limit suggests that our simulations were compromised by the decoupling effect, and that, given a specific luminosity $\Psi = 2000 \text{ erg s}^{-1}\text{g}^{-1}$, the critical neighborhood has an upper bound opacity $\kappa \approx 20$, with a lower bound opacity of $\kappa \approx 17$, as evidenced by the steady state behavior in runs with $\kappa < 17$, and the supercritical behavior in runs with $\kappa > 20$. Resolving this decoupling effect and investigating more fully the critical neighborhood would be a clear place to focus for further work.

6. Conclusions

In this work, we present the results of a set of two-dimensional numerical RHD simulations of a self-gravitating, isothermal atmosphere with a Gaussian radiation source at the midplane. This idealized model follows Krumholz & Thompson (2012) and Davis et al. (2014), but we explore the full-planar solution and employ the M_1 closure relation of Levermore (1984). We use the *Hyperion* code of Skinner & Ostriker (2013), an extension of the *Athena* code of Gardiner & Stone (2008) to evolve the RHD equations through time over our problem domain. We employ an isothermal EOS and a spatially-uniform opacity. Each

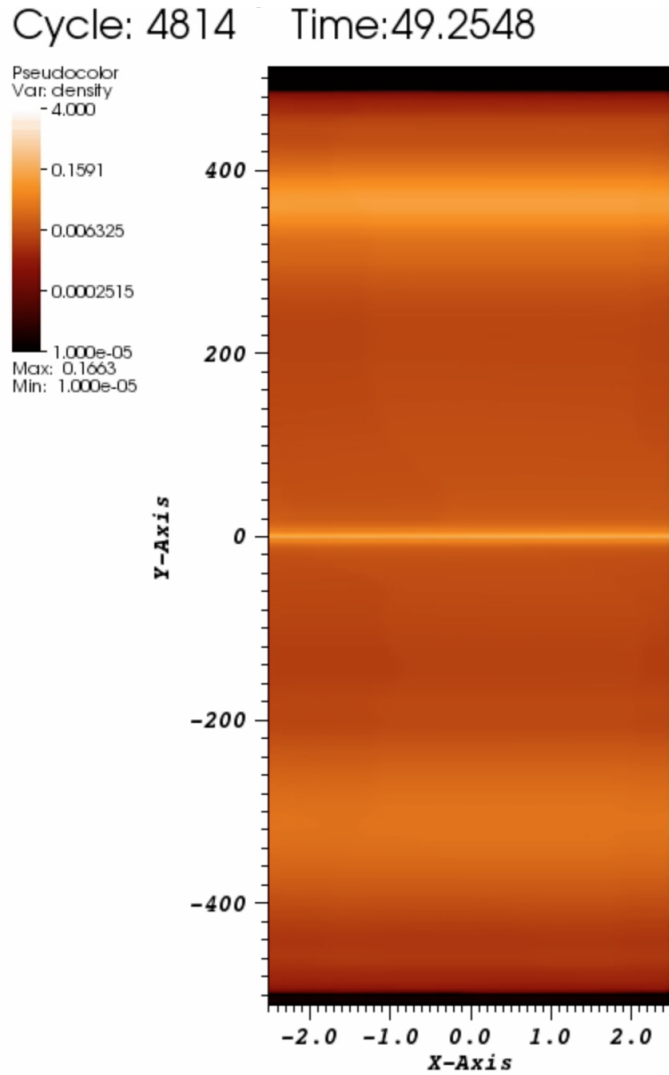


Fig. 6.— This figure shows the unbound escape of gas from the grid from the run E70K25S100, which had $\kappa = 25$. This value of κ bypasses the decoupling behavior. There is no oscillation and the gas is ejected from the simulation domain.

simulation is parameterized in terms of the opacity, κ ; the fraction of mass in the plane, ϵ_* ; and the surface density Σ . The parameter with the greatest outcome on the dynamics of the simulation is κ , as it dictates the strength of radiation and matter coupling. We explore values of κ between 5 and 25 g cm⁻², ϵ_* between 0.5 and 0.7, and adopt a characteristic value of 100 for Σ . We evolve each simulation to 250 t_{cross} , the crossing time for one scale height in the absence of radiation. The models are initialized with a relaxed density profile that incorporates both the self-gravitational potential of the gas and the static potential of the mass fixed to the plane, as well as with subsonic turbulent velocity perturbations.

Our simulations demonstrate two limits: a stable, oscillatory, regime for $\kappa < 17$, and a supercritical unstable regime for $\kappa > 20$. However, our simulations in the intermediate regime are confounded by the presence of a decoupling effect, where the bulk of the mass is unphysically ejected from the grid. Whether this effect results from some limitation of our model or an error in implementation is as yet unclear. Still, the presence of these limits hints at the existence of some interesting behavior in the intermediate regime, especially where $F_{\text{Edd,plane}} > 1$ and $F_{\text{Edd},\infty} < 1$. If observed, the presence of significant outflows in that intermediate regime would suggest that for dusty clouds, reprocessed radiation feedback may be a significant driver of turbulence. The stable results for smaller values of κ suggest that for typical clouds where $\kappa < 10 \text{ cm}^2 \text{ g}^{-1}$, reprocessed radiation alone is unlikely the account for the star formation efficiency.

I thank my advisors Eve Ostriker and Aaron Skinner for their support and help throughout this project. I also thank PICSciE for the use of the Tiger and Tigress supercomputers which were used to conduct our simulations and visualize the results. I also extend thanks to the other Astrophysical Sciences majors who helped keep me company while working on this paper.

REFERENCES

- Batten, P., Clarke, N., Lambert, C., & Causon, D. M. 1997, On the Choice of Wavespeeds for the HLLC Riemann Solver, *SIAM J. Sci. Comput.*, 18, 1553
- Davis, S. W., Jiang, Y.-F., Stone, J. M., & Murray, N. 2014, Radiation Feedback in ULIRGs: Are Photons Movers and Shakers?, *ApJ*, 796, 107
- Gardiner, T. A., & Stone, J. M. 2008, An unsplit Godunov method for ideal MHD via constrained transport in three dimensions, *Journal of Computational Physics*, 227, 4123
- Gnedin, N. Y., & Abel, T. 2001, Multi-dimensional cosmological radiative transfer with a Variable Eddington Tensor formalism, *New A*, 6, 437
- Gong, H., & Ostriker, E. C. 2013, Implementation of Sink Particles in the Athena Code, *ApJS*, 204, 8
- González, M., Audit, E., & Huynh, P. 2007, HERACLES: a three-dimensional radiation hydrodynamics code, *A&A*, 464, 429
- Kippenhahn, R., Weigart, A., & Weiss, A. 2012, Stellar Structure and Evolution, 2nd edn. (Springer)
- Krumholz, M. R. 2014, The big problems in star formation: The star formation rate, stellar clustering, and the initial mass function, *Phys. Rep.*, 539, 49
- Krumholz, M. R., & Thompson, T. A. 2012, Direct Numerical Simulation of Radiation Pressure-driven Turbulence and Winds in Star Clusters and Galactic Disks, *ApJ*, 760, 155
- Leroy, A. K., Walter, F., Brinks, E., et al. 2008, The Star Formation Efficiency in Nearby Galaxies: Measuring Where Gas Forms Stars Effectively, *AJ*, 136, 2782

- Levermore, C. D. 1984, Relating Eddington factors to flux limiters., *J. Quant. Spec. Radiat. Transf.*, 31, 149
- Mac Low, M.-M., & Klessen, R. S. 2004, Control of star formation by supersonic turbulence, *Reviews of Modern Physics*, 76, 125
- Pomraning, G. C. 1984, Higher order Levermore theory., *J. Quant. Spec. Radiat. Transf.*, 32, 185
- Rosdahl, J., Schaye, J., Teyssier, R., & Agertz, O. 2015, Galaxies that shine: radiation-hydrodynamical simulations of disc galaxies, *MNRAS*, 451, 34
- Skinner, M. A., & Ostriker, E. C. 2013, A Two-moment Radiation Hydrodynamics Module in Athena Using a Time-explicit Godunov Method, *ApJS*, 206, 21
- . 2015, Numerical Simulations of Turbulent Molecular Clouds Regulated by Reprocessed Radiation Feedback from Nascent Super Star Clusters, *ApJ*, 809, 187
- Stone, J. M., & Gardiner, T. 2009, A simple unsplit Godunov method for multidimensional MHD, *New A*, 14, 139
- Stone, J. M., Gardiner, T. A., Teuben, P., Hawley, J. F., & Simon, J. B. 2008, Athena: A New Code for Astrophysical MHD, *ApJS*, 178, 137
- Toro, E. F. 1997, Riemann solvers and numerical methods for fluid dynamics : a practical introduction (Berlin, New York: Springer)